Chemical Science

ROYAL SOCIETY OF CHEMISTRY

EDGE ARTICLE

View Article Online
View Journal | View Issue

Cite this: *Chem. Sci.*, 2026, **17**, 4116

All publication charges for this article have been paid for by the Royal Society of Chemistry

Received 15th November 2025
Accepted 22nd December 2025

DOI: 10.1039/d5sc08926c

rsc.li/chemical-science

Highly efficient CO_2 hydrogenation to long-chain linear α-olefins *via* CO intermediate enrichment over Na/FeMn/ZrO_2 catalysts

Kangzhou Wang, *[a] Tong Liu,[b] Pengqi Hai,[a] Shunnosuke Fujii,[c] Chufeng Liu,[c] Hanyao Song,[c] Caixia Zhu,[d] Guangbo Liu,[de] Jianli Zhang, *[b] Zhou-jun Wang *[bf] and Noritatsu Tsubaki *[c]

Although significant progress has been made in the oriented conversion of CO_2 to long-chain linear α-olefins (LAOs), cooperatively regulating C–O bond activation and C–C coupling *via* tailored catalyst microstructures remains a persistent challenge. Herein, a highly efficient Na/FeMn/ZrO_2 catalyst has been fabricated through a covalent anchoring strategy, which achieves a LAOs/C_{4+} selectivity of 68% and an O/P ratio of 5.1 in CO_2 hydrogenation to LAOs. There is a pronounced interaction between Fe species and $MnCO_3$ in Na/FeMn/ZrO_2 catalysts, which promotes the formation and stabilization of iron carbides. Meanwhile, Fe_5C_2–ZrO_2 interfaces possess strong adsorption capacity for CO intermediates, resulting in the accumulation of generated CO on the Fe_5C_2 active sites. The higher CO concentration on the Fe_5C_2–ZrO_2 interface is beneficial to the C–C coupling reaction, thereby significantly improving the production of high-value olefins. These results will provide a theoretical basis and guidance for developing efficient catalysts for the oriented conversion of CO_2 to LAOs.

Introduction

With rapid economic development, fossil energy consumption continues to rise, emitting substantial anthropogenic carbon dioxide (CO_2) into the environment and causing serious environmental consequences.[1–5] Directly converting CO_2 into chemicals *via* integration with green hydrogen technology not only reduces overdependence on fossil fuels and alleviates CO_2-induced environmental problems, but also provides an effective strategy for CO_2 resource utilization and high value-added chemical production.[6–9] CO_2 hydrogenation can produce CO,[10] light olefins,[11,12] gasoline,[13] methanol,[14] jet fuels,[15] and long-chain linear α-olefins.[16] Among these products, long chain linear α-olefins (LAOs, $C_{4+}^{=}$ a terminal carbon–carbon double bond) are important chemical intermediates that are used in synthetic lubricants, new polymers, high-octane gasoline, corrosion inhibitors, and agricultural chemicals.[17–19] Currently, LAOs are mostly generated by thermal cracking of petroleum resources. Therefore, the oriented conversion of CO_2 coupled with green hydrogen to LAOs is important for the sustainable development of feedstocks.

CO_2 hydrogenation to LAOs mainly involves the reverse water–gas shift (RWGS) reaction and C–C coupling reaction. In this process, CO_2 is first activated to CO *via* RWGS, and then LAOs are obtained through C–C coupling.[20,21] Fe-based catalysts are widely used for CO_2 hydrogenation to LAOs due to their combination of Fe-oxides for the RWGS reaction and Fe-carbides for the C–C coupling reaction, as well as low CH_4 selectivity.[22,23] Meanwhile, the modified Fe-based catalyst exhibited excellent catalytic activity and olefin selectivity in CO_2 hydrogenation reactions.[24,25] This demonstrated the excellent potential of modified Fe-based catalysts in CO_2 hydrogenation to LAOs. However, the generated H_2O and CO_2 can oxidize the Fe carbides, thereby weakening the C–C bond coupling ability and resulting in insufficient LAOs selectivity. Therefore, the rational construction of Fe-based catalysts for the CO_2 hydrogenation to LAOs is essential to improve LAOs selectivity.

Currently, research on Fe-based catalysts for CO_2 hydrogenation to LAOs mainly focuses on promoter modification, catalyst structure optimization, and active-site environment modulation.[26–31] The Zn promoter reduced the particle size of Fe-based catalysts and increased the adsorption of H_2, thus

[a]*School of Materials and New Energy, Ningxia University, Yinchuan 750021, Ningxia, China. E-mail: kangzhou_wang@nxu.edu.cn*

[b]*State Key Laboratory of High-efficiency Utilization of Coal and Green Chemical Engineering, College of Chemistry & Chemical Engineering, Ningxia University, Yinchuan 750021, Ningxia, China. E-mail: zhangjl@nxu.edu.cn*

[c]*Department of Applied Chemistry, School of Engineering, University of Toyama, Gofuku 3190, Toyama 930-8555, Japan. E-mail: tsubaki@eng.u-toyama.ac.jp*

[d]*Qingdao Institute of Bioenergy and Bioprocess Technology, Chinese Academy of Sciences, Qingdao 266101, China*

[e]*College of Chemical Engineering, Qingdao University of Science and Technology, 53 Zhengzhou Road, Qingdao 266042, China*

[f]*State Key Laboratory of Chemical Resource Engineering, Beijing Key Laboratory of Energy Environmental Catalysis, Beijing University of Chemical Technology, Beijing, 100029, China. E-mail: wangzj@mail.buct.edu.cn*

improving CO_2 hydrogenation activity.[32] The Na promoter efficiently enhanced CO* and H* activation, facilitated C–C coupling, and suppressed the secondary hydrogenation of olefins, thereby improving both catalytic activity and LAOs selectivity.[33] Meanwhile, the Na promoter could be enriched on the catalyst surface, which can improve olefin selectivity by inhibiting the secondary hydrogenation of primary olefins.[34] Sr and Na co-modified Fe-based catalysts exhibited stable catalytic performance in CO_2 hydrogenation to LAOs. $SrCO_3$ promoted the formation and stabilization of the FeC_x phase. Meanwhile, the Sr promoter strengthened electronic interactions between Na and Fe, thereby improving C–O bond dissociation and C–C coupling.[35] A Cu–Fe catalyst consisting of Cu, Fe-oxides and Fe carbides achieved a $C_{4+}^{=}$ selectivity of 66.9% under atmospheric pressure. The synergistic interaction between Fe_5C_2 and the Cu–Fe_5C_2 interface promoted the generation of long-chain olefins.[36]

Although significant progress has been made in CO_2 hydrogenation to LAOs, effective control of C–O bond activation and C–C bond coupling through interface structures remains challenging. Developing highly efficient catalysts to enhance C–C coupling is crucial for improving LAOs selectivity. By modulating promoter content, the active-phase composition (Fe_3O_4 and Fe_5C_2) can be effectively regulated to optimize RWGS/FTS reaction matching. Fe–Mn–K catalysts exhibited excellent catalytic performance with a CO_2 conversion of 32.9% and LAOs selectivity of 45.7%.[37] Significant progress has been made in understanding the stabilizing and promoting effects of Mn on iron carbides in CO_2 hydrogenation reactions. The Mn promoter significantly reduced the rates of reduction and carbonization reactions, inducing pronounced reaction-induced evolution of the Fe_5C_2 phase. A surface layer of MnO converting Fe_5C_2 effectively inhibited CH_4 formation, while promoting the production of light olefins and C_{5+} hydrocarbons.[38] Guo *et al.*[30] employed multiple *in situ* techniques to reveal the structural evolution of Fe-based catalysts during CO_2 hydrogenation to hydrocarbons. In the initial reduction phase, Fe species undergo carbonization to form Fe_3C, which subsequently transforms into Fe_5C_2. The generated H_2O during CO_2 hydrogenation to LAOs could oxidize Fe_5C_2 to the Fe_3O_4 phase. The Fe_5C_2–ZrO_2 interfacial structure enhanced the adsorption of key CO intermediates, forming a CO-enriched microenvironment on the Fe_5C_2 active phase surface. This significantly increases the partial pressure of CO on the Fe_5C_2 phase, thereby reducing the adsorption energy of H_2O on the Fe_5C_2 surface.[39,40] Consequently, it effectively improved catalyst stability and C–C coupling capability. The introduction of Mn promoted the dispersion of Fe species and enhanced the formation of Fe oxides, while the addition of the K promoter favored the generation of Fe carbides, thus improving carbon-chain growth capability. The incorporation of Mn and K effectively modulates the balance between the RWGS and FTS reactions by promoting the formation and conversion of CO intermediates.[37,41] In FeZr catalysts, oxygen vacancies in ZrO_2 promote CO_2 adsorption and activation.[42] Although significant progress has been achieved with K/FeMn catalysts in CO_2 hydrogenation to LAOs, research has mainly focused on regulating the RWGS and FTS active sites through the Mn promoter to achieve high olefin selectivity. In contrast, K–FeZr catalysts primarily modulate CO_2 adsorption and H_2 dissociation through oxygen vacancies, exhibiting excellent selectivity toward light olefins in CO_2 hydrogenation. Therefore, the Fe_5C_2–ZrO_2 interfacial structure can create a CO-enriched microenvironment at the Fe_5C_2 active sites by utilizing the strong CO adsorption capacity of oxygen vacancies on the ZrO_2 surface. This effectively increases the partial pressure of CO on the Fe_5C_2 surface and reduces the adsorption energy of H_2O, thereby suppressing the oxidation of the Fe_5C_2 active phase by H_2O and significantly enhancing the C–C coupling capability.[43] Meanwhile, the interfacial structure not only facilitates the transport of key intermediate species, but also lowers the activation energy barrier for C–C coupling.[36] Therefore, constructing Fe_5C_2–ZrO_2 interfacial catalysts should effectively promote LAOs synthesis in CO_2 hydrogenation.

In this work, we report a Na/FeMn/ZrO_2 catalyst that demonstrated high catalytic performance for CO_2 hydrogenation to LAOs. Under reaction conditions of 320 °C, 1.5 MPa, and 7500 mL g_{cat}^{-1} h^{-1}, it achieved a LAOs selectivity in C_{4+} hydrocarbons of 68.0% and an O/P ratio of 5.1. The structure–performance relationships were revealed by various characterization techniques. The strong CO adsorption capacity at the Fe_5C_2–ZrO_2 interface enriched CO intermediates on Fe_5C_2 active sites, promoting C–C coupling reactions. Meanwhile, strong interfacial interactions enhanced synergy among various active sites, resulting in superior selectivity for high-value olefins.

Results and discussion

Active phase characterization

The active phase composition of the catalysts was analyzed by XRD. The calcined samples of Fe, Na/Fe, and Na/FeMn exhibited characteristic diffraction peaks of the Fe_2O_3 phase (JCPDS, 33-0664) (Fig. S1). However, the diffraction peak intensities of the Fe_2O_3 phase in the Na/FeMn/SiO_2 and Na/FeMn/ZrO_2 catalysts were much weaker (Fig. S1). XRD patterns of the reduced catalysts are shown in Fig. 1. The characteristic diffraction peaks of the Fe phase (JCPDS, 06-0696) appeared in the reduced Fe and Na/Fe catalysts, while a mixed phase of Fe, $FeMnO_x$, and Mn_2O (JCPDS, 07-0230) appeared in the reduced Na/FeMn catalyst. However, no significant Fe phases were detected in

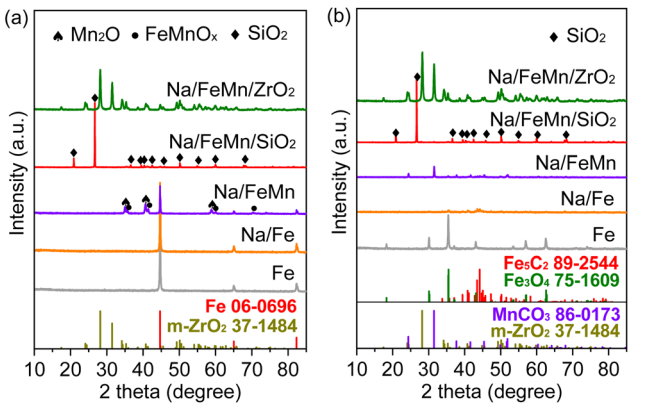

Fig. 1 XRD patterns of the reduced (a) and spent (b) catalysts.

the reduced Na/FeMn/SiO_2 and Na/FeMn/ZrO_2 catalysts, indicating that the reduced Fe species were uniformly dispersed on SiO_2 and ZrO_2. Only characteristic diffraction peaks of the Fe_3O_4 phase (JCPDS, 75-1609) were detected in the spent Fe catalysts. Compared with the pure Fe catalyst, the Na/Fe catalyst exhibited a weak Fe_5C_2 phase (JCPDS, 89-2544), indicating that the Na promoter was beneficial to the formation of the Fe_5C_2 phase.[44] The $MnCO_3$ phase (JCPDS, 86-0173) appeared in the spent Na/FeMn catalyst, which stabilized the active phase and improved the catalytic activity owing to the thermal stability and electronic interactions of alkaline earth metal carbonates.[45] No significant Fe carbide phase was detected in the spent Na/FeMn/SiO_2 catalysts, because the interaction between Fe species and SiO_2 hydroxyl groups from Fe–O–Si bonds was unfavorable for the formation of iron carbides. However, both Fe_3O_4 and Fe_5C_2 phases (JCPDS, 89-2544) appeared in the spent Na/FeMn/ZrO_2 catalyst, indicating that Fe species can be further carbonized to form Fe_5C_2. The strong interaction between Fe and ZrO_2 could promote iron carbide formation.[40]

In situ XRD analysis was performed to reveal the phase evolution during H_2 reduction and CO_2 hydrogenation reaction processes over the Na/FeMn/ZrO_2 catalyst. The characteristic diffraction peaks of Fe_2O_3 and ZrO_2 were mainly detected on the Na/FeMn/ZrO_2 catalyst (Fig. S2). The characteristic diffraction peaks of Fe_2O_3 were weak, indicating that the Fe species were uniformly distributed on ZrO_2. The interaction between the complex (formed by the ethylene diamine tetraacetic acid and Fe species) and hydroxyl groups at oxygen vacancies of ZrO_2 was reported to form small sized Fe_2O_3.[46] Increasing the reduction temperature to 350 °C caused disappearance of Fe_2O_3 diffraction peaks with no detectable Fe_3O_4 diffraction peaks (Fig. 2a). That is, Fe_2O_3 could be completely reduced at 400 °C and the reduced Fe species were uniformly dispersed on the ZrO_2 surface. After reduction, the system was cooled to 320 °C and then the feedstock ($H_2/CO_2 = 3$) was introduced. As the reaction progressed, the characteristic peaks of Fe_3O_4, Fe_5C_2, and $MnCO_3$ appeared. The reappearance of Fe_3O_4 was attributed to the oxidation of FeO or Fe during the reaction (Fig. 2b). The resultant Fe_3O_4 and Fe_5C_2 were the active sites for the RWGS and FTS reactions, respectively. Importantly, ZrO_2 remained unchanged in its monoclinic phase, indicating its stable presence during the CO_2 hydrogenation reaction (Fig. S3).

Morphology and textural characteristics

SEM images clearly exhibited the microscopic morphology of the catalysts. The fresh Na/FeMn/ZrO_2 catalysts exhibited a stack of spherical nanoparticles around 50 nm (Fig. S4). Compared with the fresh Na/FeMn/ZrO_2 catalyst, the spent catalyst displayed larger particles and elongated crystals, due to the formation of some $MnCO_3$ and $FeMnO_x$ species during the reaction. The microstructure of fresh and spent Na/FeMn/ZrO_2 catalysts was further characterized using the HR-TEM technique, and the results are shown in Fig. 3 and S5. The fresh Na/FeMn/ZrO_2 catalysts possessed an irregular crystal structure with rough edges, and the particle size of the Na/FeMn/ZrO_2 catalysts increased after the reaction (Fig. 3a and c). The intimacy of catalyst components had a great influence on the catalyst performance. The HAADF-STEM images and the corresponding EDS elemental maps of the fresh and spent Na/FeMn/ZrO_2 catalysts were analyzed in detail. The elements Fe, Mn, and Na in the Na/FeMn/ZrO_2 catalysts were almost uniformly distributed on the ZrO_2 support (Fig. 3e and S5).

Meanwhile, Na, Fe, Mn, and Zr species exhibited relatively close contact (Fig. S6). The closely packed $MnCO_3$ effectively stabilized the Fe_5C_2 active phase, inhibiting the oxidation that generated H_2O molecules and thereby promoting C–C coupling reactions.[47] To further characterize the Fe_5C_2–ZrO_2 interface structure, EDS mapping of Fe and Zr elements was performed (Fig. S7). The mapping of Fe and Zr in the Na/FeMn/ZrO_2 catalyst clearly revealed an interfacial structure.

To further elucidate the elemental composition of the catalyst, ICP analysis was performed, and the results are summarized in Table S1. The elemental compositions of the Na/FeMn, Na/FeMn/SiO_2, and Na/FeMn/ZrO_2 catalysts were found to be consistent with theoretical values. The surface area and pore size distribution of the synthesized catalysts were analyzed

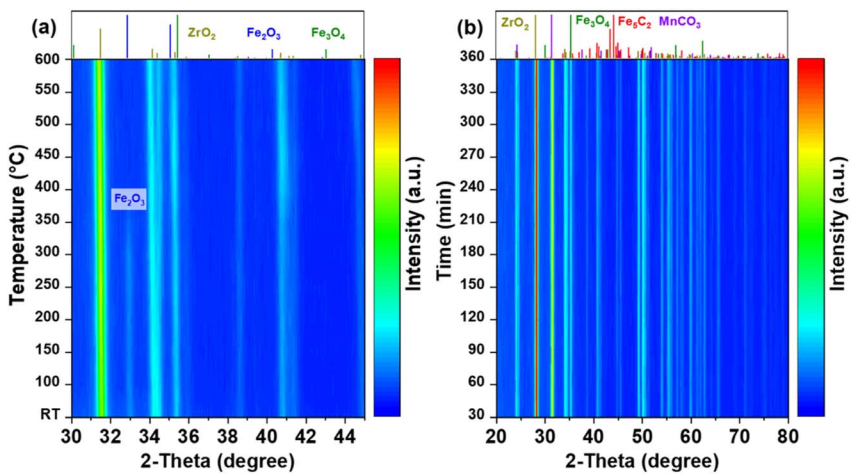

Fig. 2 *In situ* XRD patterns of the Na/FeMn/ZrO_2 catalyst during H_2 reduction (a) and the CO_2 hydrogenation reaction (b). Reduction process: pure H_2, 30 mL min^{-1}. Reaction process: $H_2/CO_2 = 3$, 320 °C, 30 mL min^{-1}, atmospheric pressure.

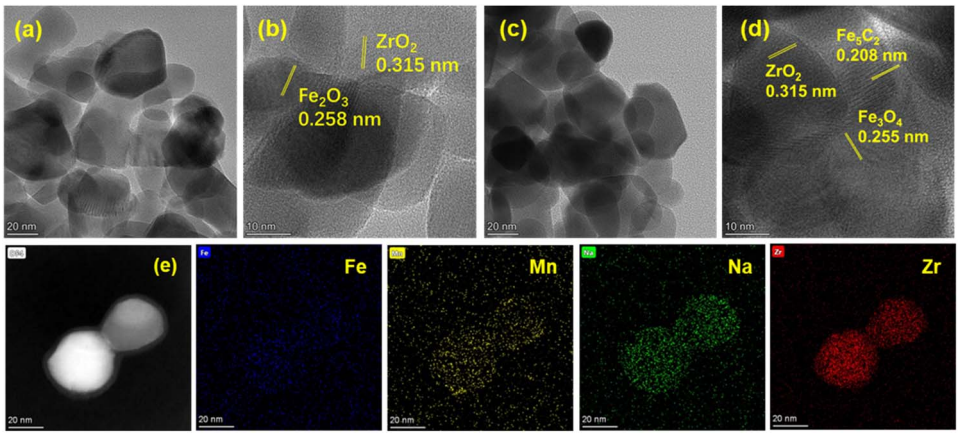

Fig. 3 TEM images of the fresh (a and b) and spent (c and d) Na/FeMn/ZrO_2 catalysts. STEM image of the spent Na/FeMn/ZrO_2 catalyst (e) and the corresponding EDS elemental mapping images.

using N_2 adsorption–desorption measurements, and the results are summarized in Table S2. The addition of the Na promoter to the Fe catalyst increased its specific surface area (from 23.7 m^2 g^{-1} to 25.0 m^2 g^{-1}) and enlarged the average pore size from 11.5 nm to 13.8 nm. Compared with Na/Fe, Na/FeMn exhibited smaller specific surface area, pore size, and pore volume due to nanoparticle aggregation caused by the promoter. Na/FeMn/SiO_2 catalysts had the smallest specific surface area and pore size. Relative to Na/FeMn, Na/FeMn/ZrO_2 showed significantly higher specific surface area and pore volume alongside reduced pore size. These changes indicate that ZrO_2 improved the dispersion of active sites by increasing the specific surface area, which was beneficial for the reaction and diffusion of feedstocks/intermediates.

Chemical state, reduction and chemisorption behavior

To determine the chemical state of the catalyst, we carried out XPS analysis of the spent catalysts with the results shown in Fig. 4. The binding energies of the Fe 2p spectra of all spent catalysts exhibited two characteristic peaks at 710.8 eV and 723.9 eV, which were assigned to Fe $2p_{3/2}$ and Fe $2p_{1/2}$ of iron oxide species, respectively (Fig. 4a).[48] The Na/Fe, Na/FeMn, Na/FeMn/SiO_2, and Na/FeMn/ZrO_2 catalysts displayed characteristic peaks at 706.8 eV, which were attributed to Fe carbide species.[48] No characteristic peaks of Fe carbide were detected in the fresh catalyst and the reduced catalyst. Meanwhile, no such signal was detected in the Fe catalyst, indicating that Na and Mn promoters play a crucial role in the formation of Fe carbide species. Mn 2p XPS spectra exhibited two characteristic peaks at 641.7 eV and 653.5 eV, which corresponded to Mn $2p_{3/2}$ and Mn $2p_{1/2}$ of manganese oxide species, respectively (Fig. S8). However, the spent catalysts displayed two shoulder peaks, which were attributed to the characteristic features of Mn^{2+} in $MnCO_3$ species (Fig. S8). Notably, the C 1s binding energy of Na/FeMn, Na/FeMn/SiO_2, and Na/FeMn/ZrO_2 catalysts shifted to 289.2 eV, which was higher than that of Fe and NaFe catalysts (at 288.7 eV) (Fig. 4b). The apparent change in binding energy further revealed strong electron transfer and interfacial interaction between Fe species and Mn species.[30] The O 1s spectra displayed two characteristic peaks corresponding to oxygen vacancy and lattice oxygen, appearing at 532.1 and 529.6 eV, respectively (Fig. 4c and S11).[49] Fresh Na/FeMn samples show higher oxygen vacancies and lattice oxygen, while fresh Na/FeMn/SiO_2 samples predominantly contain lattice oxygen. After reduction, the oxygen vacancies in the Na/FeMn catalyst decreased significantly, while those in Na/FeMn/SiO_2 and Na/FeMn/ZrO_2 samples increased. The oxygen vacancy was beneficial to the CO_2 activation.[50] Although the spent Na/FeMn/SiO_2 sample possessed abundant oxygen vacancies, its catalytic activity and olefin selectivity were relatively low. This was primarily attributed to Fe species interacting with silicon hydroxyl groups to form Fe_2SiO_4, which was difficult to further reduce into Fe_5C_2, resulting in insufficient C–C coupling active sites in the Na/FeMn/SiO_2 catalyst.[51,52] The Zr 3d binding energy of Na/FeMn/ZrO_2 exhibited two peaks at 183.8 eV and 181.4 eV, which were attributed to ZrO_2 species (Fig. S12). The binding energy of the Si 2p spectra of Na/FeMn/SiO_2 appeared at 101.8 eV, which was associated with SiO_2 species (Fig. S13). These results indicated that Mn and ZrO_2 promoted the dissociation of lattice oxygen to generate oxygen vacancies during the reduction process, thereby improving CO intermediate adsorption and C–C coupling. The surface elemental compositions of the spent catalyst are listed in Table S3. Compared with Fe, the Na/Fe catalyst exhibited lower surface Fe content and higher C content, indicating that the Na promoter enhanced the carbonization capability of Fe species. With the introduction of the Mn promoter, the surface Fe content decreased, which was attributed to the Mn species migrating to the surface of Fe species.[38] Compared with the Na/FeMn/SiO_2 catalyst, the Na/FeMn/ZrO_2 catalyst exhibited higher carbon content, indicating greater susceptibility to carbonization and formation of Fe_5C_2 active sites.

H_2-TPR experiments were performed to evaluate the interactions between the species. In Fig. 4d, H_2 consumption peaks at 365 °C and 527 °C for the Fe catalyst represented the gradual reduction of Fe_2O_3 to Fe. Specifically, the H_2 consumption peak at 365 °C was attributed to the reduction of Fe_2O_3 to Fe_3O_4, while the broad peak near 527 °C was attributed to the

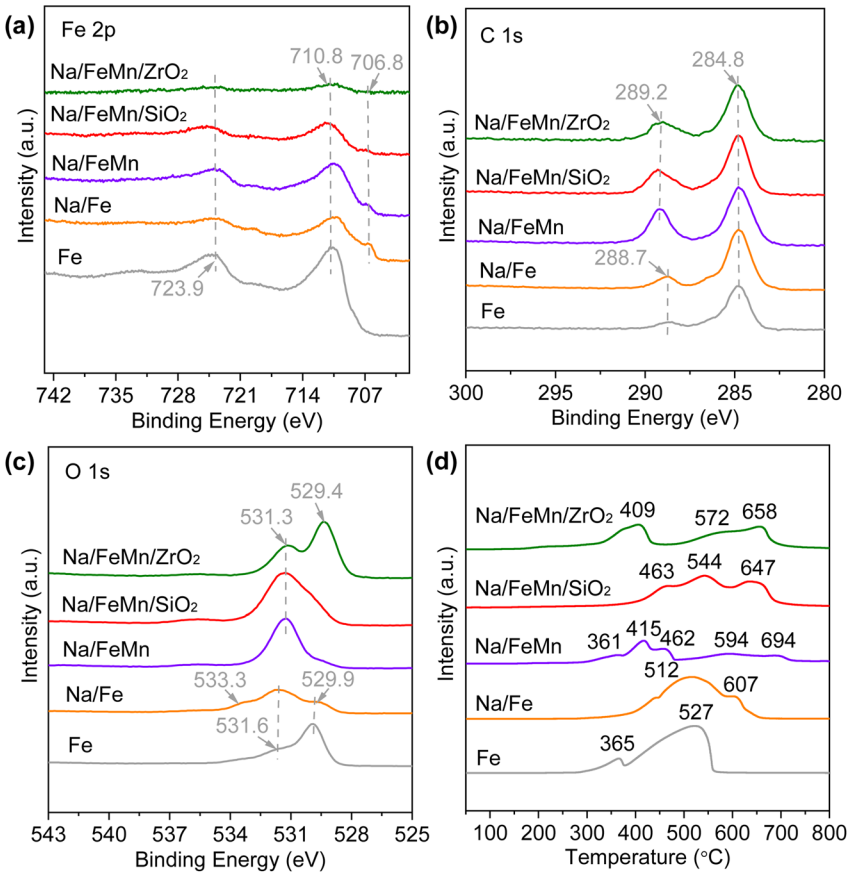

Fig. 4 Fe 2p (a), C 1s (b), and O 1s (c) XPS spectra of the spent catalysts. (d) H_2-TPR profiles of the synthesized catalysts.

reduction of Fe_3O_4 to FeO and the further reduction of FeO to Fe. Compared with the Fe catalyst, Na/Fe exhibited a H_2 consumption peak with higher temperature, indicating that the Na promoter inhibited the reduction of Fe_2O_3. MnO_2 samples exhibited three reduction peaks at 308 °C, 422 °C, and 510 °C (Fig. S14). The reduction peak at 361 °C for Na/FeMn was weakened, while the high-temperature peaks increased, indicating that the transition metal enhanced the Fe–O bond energy.[53] For the Na/FeMn catalyst, H_2 consumption peaks near 361 °C and 462 °C were attributed to the reduction of Mn species. Relative to the Na/Fe catalyst, the Na/FeMn catalyst exhibited significantly lower H_2 consumption, with all Fe species reduction peaks shifting to higher temperatures. This indicates that Mn species strengthened the Fe–O bond energy.[54] In comparison, the reduction peaks of the Na/FeMn/SiO_2 catalysts all shifted to high temperature, which was attributed to the formation of the Fe–O–Si bond.[55] Compared with Na/FeMn catalysts, the reduction peak of the Na/FeMn/ZrO_2 catalyst shifted to a lower temperature, which was beneficial to the reduction of Fe species.[53] This shift was attributed to ZrO_2 enhancing the migration and reactivity of hydrogen species.[56] These results further indicated strong interactions among Fe, Mn, and Zr species, which had a positive effect on the stability of iron carbide species. The H_2 consumption of as-prepared catalysts is summarized in Table S4. Compared with the Fe catalyst, the Na/Fe catalyst exhibited lower low-temperature H_2 consumption and higher high-temperature H_2 consumption. The introduction of the Mn promoter enhanced the formation of $FeMnO_x$ spinel, which hindered the reduction of both Fe and Mn species, leading to decreased H_2 consumption. The H_2 consumption of Na/FeMn/SiO_2 and Na/FeMn/ZrO_2 decreased due to reduced Fe content from the introduced supports. Compared with Na/FeMn/SiO_2, the Na/FeMn/ZrO_2 catalyst exhibited higher low-temperature H_2 consumption, while lower high-temperature consumption, indicating greater susceptibility to H_2 reduction.

To elucidate the CO adsorption of the Na/FeMn/ZrO_2 catalyst, CO-TPD analysis was performed on reference ZrO_2 and Na/FeMn/ZrO_2 catalysts (Fig. S15). The ZrO_2 sample exhibited a weak CO desorption peak at 291 °C, indicating its relatively low CO adsorption. Compared with the ZrO_2 sample, the Na/FeMn/ZrO_2 catalyst exhibited a pronounced CO desorption peak at 313 °C, indicating that the Na/FeMn/ZrO_2 catalyst with an Fe_5C_2–ZrO_2 interfacial structure possesses strong CO adsorption. The strong adsorption capacity for CO enabled the formation of a high partial pressure of CO on the surface of the Na/FeMn/ZrO_2 catalyst, thereby inhibiting the adsorption of H_2O molecules on the Fe_5C_2 active sites and effectively promoting the C–C coupling reaction.[43] CO-DRIFTS was employed to further investigate the adsorption configuration and strength of CO on the surface of the Na/FeMn/ZrO_2 catalyst (Fig. S16). The adsorption and desorption spectra of the Na/FeMn/ZrO_2 catalyst exhibited peaks at 2170 cm^{-1} and

2118 cm^{-1}, respectively, which was attributed to the adsorption of gaseous CO. Peaks observed at 2068 cm^{-1}, 2054 cm^{-1}, and 2031 cm^{-1} correspond to linear CO adsorption. These linear CO adsorption peaks markedly intensify with extended adsorption time. The adsorbed CO could enhance the partial pressure of CO at the Fe_5C_2 active sites, thereby promoting C–C coupling reactions.[43,57]

The effective adsorption of CO_2 on the active sites of the catalysts could promote the activation of C–O bonds and the generation of CO intermediates. CO_2-TPD analysis was employed to elucidate CO_2 adsorption behavior of the catalysts (Fig. S17). The Na/Fe catalyst displayed two desorption peaks, where the low- and high-temperature peaks were attributed to the interaction of CO_2 molecules with weak and strong base sites, respectively. Compared with the Na/Fe catalyst, Na/FeMn catalysts exhibited stronger CO_2 desorption peaks at 200 °C, suggesting that Na and Mn promoters enhanced CO_2 adsorption. The desorption peak of CO_2 for the Na/FeMn/SiO_2 catalyst was significantly weakened, indicating that the Na/FeMn/SiO_2 catalyst had a weaker adsorption capacity for CO_2.[58] The Na/FeMn/ZrO_2 catalyst exhibited a strong CO_2 desorption peak near 100 °C, indicating that the introduction of ZrO_2 increased CO_2 adsorption capacity despite weak binding strength. These results indicated that the introduction of Mn species and ZrO_2 modulated the amount and strength of CO_2 adsorption.[59] The suitable CO_2 adsorption on catalyst active sites promoted the generation of Fe-carbide active phases, which improved the yield of high-value olefins.

Mössbauer spectroscopy analysis

^{57}Fe Mössbauer spectroscopy of the spent Na/FeMn/ZrO_2 catalysts further identified the Fe species in the catalysts, and the results are shown in Fig. 5. The detailed composition and comparison of the different phases are listed in Table S5. Small amounts of Fe_3O_4 species were contained in the spent Na/FeMn/ZrO_2 catalysts, which were mainly detected as Fe_5C_2(II), Fe_5C_2(I), and Fe_5C_2(III), accounting for 31.7%, 26.2%, and 29.9%, respectively.[60–62] Therefore, the synergistic effect of Fe_5C_2 and Fe_3O_4 active sites promoted the highly selective synthesis of high value olefins from CO_2 hydrogenation.

To further investigate the adsorption, activation, and dissociation strength of CO intermediates, H_2-TPSR measurements were performed on the Na/FeMn and Na/FeMn/ZrO_2 catalysts. In Fig. 5b, the Na/FeMn catalyst exhibited two CO desorption peaks, and the desorption peaks were primarily concentrated in the temperature range of 450 °C to 750 °C. Relative to Na/FeMn, Na/FeMn/ZrO_2 exhibited attenuated CO desorption intensity with peaks shifting to higher temperatures, providing evidence of strengthened CO adsorption. Consequently, substantial CO accumulated at the Fe_5C_2–ZrO_2 interface, where it rapidly migrated to Fe_5C_2 sites, facilitating C–C coupling reactions. Meanwhile, two H_2 consumption peaks appeared on the surface of the Na/FeMn catalyst. The H_2 consumption of the Na/FeMn/ZrO_2 catalyst significantly increased, indicating that the enriched CO underwent dissociation. These results indicated that the Na/FeMn/ZrO_2 catalyst with an Fe_5C_2–ZrO_2 interfacial structure could enrich CO at the interface. The enriched CO underwent dissociation and C–C coupling at Fe_5C_2 active sites, promoting CO_2 hydrogenation toward high-value olefins.

Catalytic performance

The catalytic performance of the prepared catalysts for CO_2 hydrogenation to LAOs is shown in Fig. 6. Detailed results on product distribution, O/P ratio, and LAOs yield are summarized in Table S6. The Fe catalyst exhibited a CO_2 conversion of 29.3%, a LAOs/C_{4+} ratio of 4.1%, and a LAOs yield of 0.2%. Compared with the Fe catalyst, Na/Fe displayed significantly higher CO_2 conversion and C_{5+} selectivity, alongside markedly lower CH_4 selectivity and LAOs selectivity (Fig. 6a). Na content impacts CO_2 hydrogenation by reducing the hydrogen adsorption and activation capacity, thereby reducing the coverage of hydrogen species.[63] The primary reaction of CO_2 hydrogenation is suppressed. Compared with the unpromoted Fe catalyst, Na/Fe catalysts exhibited lower selectivity toward CH_4 and C_2–C_4 hydrocarbons. The inhibitory effect of Na on CH_4 and light alkane formation could be attributed to its regulation of the electronic properties of iron carbides, which enhanced the generation of surface carbon-containing species and hydrogen-containing species.[64] Furthermore, the Na promoter was beneficial to the production of C_{5+} hydrocarbons by modulating the

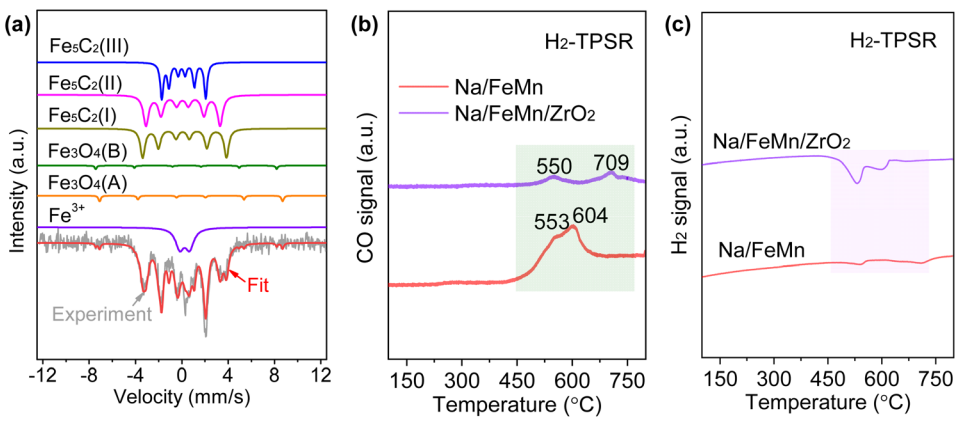

Fig. 5 ^{57}Fe Mössbauer results of the spent Na/FeMn/ZrO_2 catalyst (a); CO signal (b) and H_2 signal (c) under CO pre-adsorption and H_2-TPSR measurements.

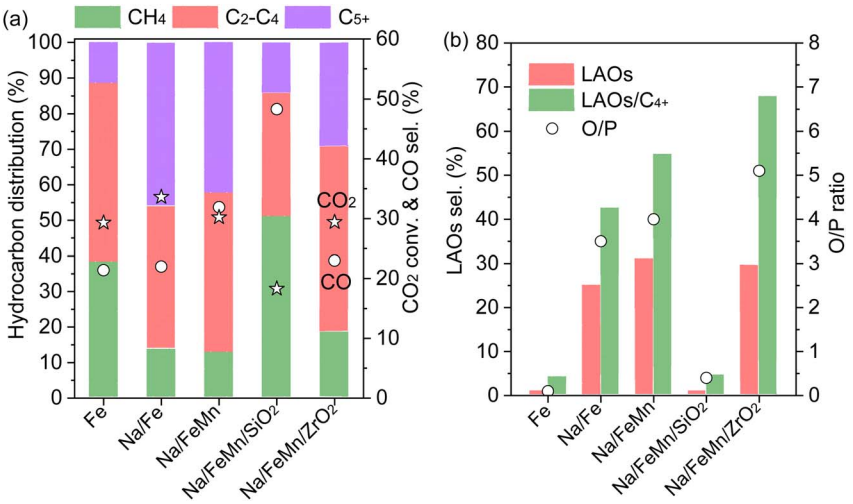

Fig. 6 Catalytic performance toward CO_2 hydrogenation. (a) The hydrocarbon distribution, CO_2 conversion, and CO selectivity. (b) LAOs selectivity, LAOs/C_{4+} ratio, and O/P ratio of catalysts. Reaction conditions: $H_2/CO_2 = 3$, 1.5 MPa, 320 °C, 7500 mL g_{cat}^{-1} h^{-1}, TOS = 10 h. The LAOs/C_{4+} ratio represents the LAO fraction within the C_{4+} hydrocarbons.

surface carbon-to-hydrogen ratio, primarily following a catalytic surface polymerization mechanism.[65] The promotion of CO disproportionation (Boudouard reaction) also increased carbonization in Na-promoted catalysts, facilitating the formation of Fe_5C_2 and accelerating C–C coupling reactions.[66] The Na/FeMn catalyst exhibited higher catalytic activity and LAOs selectivity with a CO_2 conversion of 30.2%, a LAOs/C_{4+} selectivity of 54.8%, a light olefin selectivity of 35.9%, and a LAOs yield of 6.3%. The introduction of the Na promoter decreased CH_4 selectivity from 38.2% to 22.0%, which was attributed to the electron transfer from Na to the Fe_5C_2 phase. The resulting increase in electron density at Fe sites facilitated the CO dissociation and destabilized adsorbed H atoms on the Fe surface, thereby promoting the hydrogenation of carbon species.[67] The introduction of Mn further enhanced the electron-donating ability of Na and promoted the formation of $MnCO_3$, leading to Na enrichment on the Fe_5C_2 surface and providing abundant basic sites. The steric hindrance effect induced by high-density sodium enrichment on the Fe_5C_2 surface impairs chain growth capability.[47] Studies indicated that Na and Mn synergistic effects could enhance RWGS and FTS. Nevertheless, as the Mn/Fe molar ratio increased from 1 : 3 to 1 : 1, CO selectivity reverses, suggesting that higher Mn content weakens FTS activity. Compared with the Na/Fe catalyst, the Na/FeMn catalyst exhibited lower CO_2 conversion and higher CO selectivity. This decline in activity was likely due to coverage of active sites by the Mn promoter. When Mn was added to the Na/Fe catalyst, Mn species dispersed uniformly on the Fe_5C_2 surface. The steric hindrance caused by these Mn species reduced the ability of intermediates to undergo C–C coupling on the Fe_5C_2 phase, thereby inhibiting the formation of C_{5+} hydrocarbons.[68] The suppressed C–C coupling allowed CO generated *via* RWGS to accumulate, increasing CO selectivity. These results are consistent with those reported in the literature.[68] Compared with the Na/FeMn catalyst, Na/FeMn/SiO_2 showed significantly lower CO_2 conversion and LAOs selectivity but higher CO selectivity. This resulted from different reduction/activation of Fe species, which limited chain growth active sites and prevented the generated CO from being activated to undergo C–C coupling for the formation of LAOs.[69] The Na/FeMn/ZrO_2 catalyst possessed higher CO_2 conversion and LAOs selectivity, but lower CO and CH_4 selectivity than Na/FeMn/SiO_2 (Fig. S18). Among these catalysts, the Na/FeMn/ZrO_2 catalyst possessed a higher LAOs yield of 6.7%. Importantly, the LAOs/C_{4+} selectivity and O/P ratio of the Na/FeMn/ZrO_2 catalyst reached 68.0% and 5.1, respectively (Fig. 6b). For the C_{2+} product distribution, the Fe catalyst had higher selectivity for light alkanes, while Na/Fe exhibited higher light olefin selectivity and C_{5+} alkane selectivity. With Mn promotion, the Na/FeMn catalyst showed significantly higher light olefin and C_{5+} olefin yields than Na/Fe. This indicated that Na and Mn promoters suppressed secondary hydrogenation of primary olefins, thereby boosting selectivity toward high-value olefins. Among these catalysts, the Na/FeMn/ZrO_2 catalyst possessed the highest high-value olefin selectivity (61.3%) and O/P ratio (5.1). The Fe_5C_2–ZrO_2 interfacial structure effectively enhanced the synergism among various active sites and CO intermediate adsorption. Moreover, the CO generated by the RWGS reaction on FeMn sites could be effectively adsorbed at this interface. The significantly increased CO partial pressure on Fe_5C_2 enhanced C–C coupling capability while suppressing olefin secondary hydrogenation, thereby promoting high-value olefin formation and specifically improving LAOs selectivity.

Reaction mechanism for CO_2 hydrogenation to LAOs

Compared with other investigated catalysts, Na/FeMn/ZrO_2 exhibited the best high-value olefin selectivity in CO_2 hydrogenation. To reveal the key intermediate species during the reaction, *in situ* DRIFTS analysis was performed over Na/FeMn/ZrO_2. The peaks in the wavenumber range of 2400 cm^{-1} to 2300 cm^{-1} were attributed to the adsorption of gaseous CO_2 (Fig. S19), indicating that the catalyst possessed a strong adsorption

capacity for CO_2 molecules.[25] As shown in Fig. 7, the vibrational peaks in the range of 1710–1200 cm^{-1} were assigned to the adsorbed carbonate and formate species (CO_3^*, HCO_3^* and HCOO*). These intermediates were formed through the interaction of oxygen vacancies on the catalyst surface with CO_2.[70] The vibration peak at 1672 cm^{-1} was attributed to the symmetric and asymmetric stretching vibrations of the bidentate carbonate species. As the reaction proceeded, vibration peaks corresponding to carbonate (CO_3^*) and bicarbonate (HCO_3^*) species appeared at 1370 cm^{-1} and 1308 cm^{-1}.[71] At a reaction temperature of 200 °C (Fig. 7a), the vibration peaks at 1370 cm^{-1} and 1297 cm^{-1} did not change significantly as the reaction proceeded. This result indicated that the generated CO_3^* species did not fully participate in the subsequent reaction. At a higher reaction temperature of 320 °C (Fig. 7b), the vibrational peaks of CO_3^* species gradually increased as the reaction proceeded, indicating that the initially generated CO_3^* species were rapidly involved in the subsequent reaction. CO intermediates enriched at the Fe_5C_2 active site were beneficial to the C–C coupling.

To further demonstrate CO enrichment on Fe_5C_2 active sites enabled by the Fe_5C_2–ZrO_2 interface, we compared CO adsorption energies on Fe_5C_2 and Fe_5C_2–ZrO_2 using density functional theory (DFT) calculations. To simulate the Fe_5C_2–ZrO_2 interface, we constructed $Fe_5C_2(11-2)$ on the $ZrO_2(-111)$ surface (Fig. S20). As depicted in Fig. 7c, the CO adsorption energy on Fe_5C_2 and the Fe_5C_2–ZrO_2 interface was 1.97 eV and 2.12 eV, respectively. The higher CO adsorption energy on the Fe_5C_2–ZrO_2 interface suggested stronger CO adsorption capacity. The Fe_5C_2–ZrO_2 interface promoted CO adsorption, thereby enriching CO at the Fe_5C_2 active sites. The enriched CO could accelerate the occurrence of C–C coupling reactions. To gain a deeper understanding of the reaction mechanism, we calculated the energy barrier for C–C coupling. CO_2 hydrogenation to high value olefins is a complex process involving multiple possible steps. For simplicity, we employed CH_2 + CH_2 to represent the C–C coupling reaction between CH_2 intermediates. The energy barrier for CH_2 insertion on the Fe_5C_2 surface reached up to 0.81 eV. For the Fe_5C_2–ZrO_2 interface, the energy barrier for CH_2 insertion decreased to 0.64 eV. These results indicated that the Fe_5C_2–ZrO_2 interface not only enabled CO enrichment at Fe_5C_2 active sites, but also lowered the C–C coupling energy barrier, thereby promoting C–C coupling reactions toward high-value olefin production. Therefore, the possible reaction pathways for CO_2 hydrogenation to high-value olefins on Na/FeMn/ZrO_2 catalysts with Fe_5C_2–ZrO_2 interface structures are proposed in Fig. 7e. Notably, the synergistic action of each active

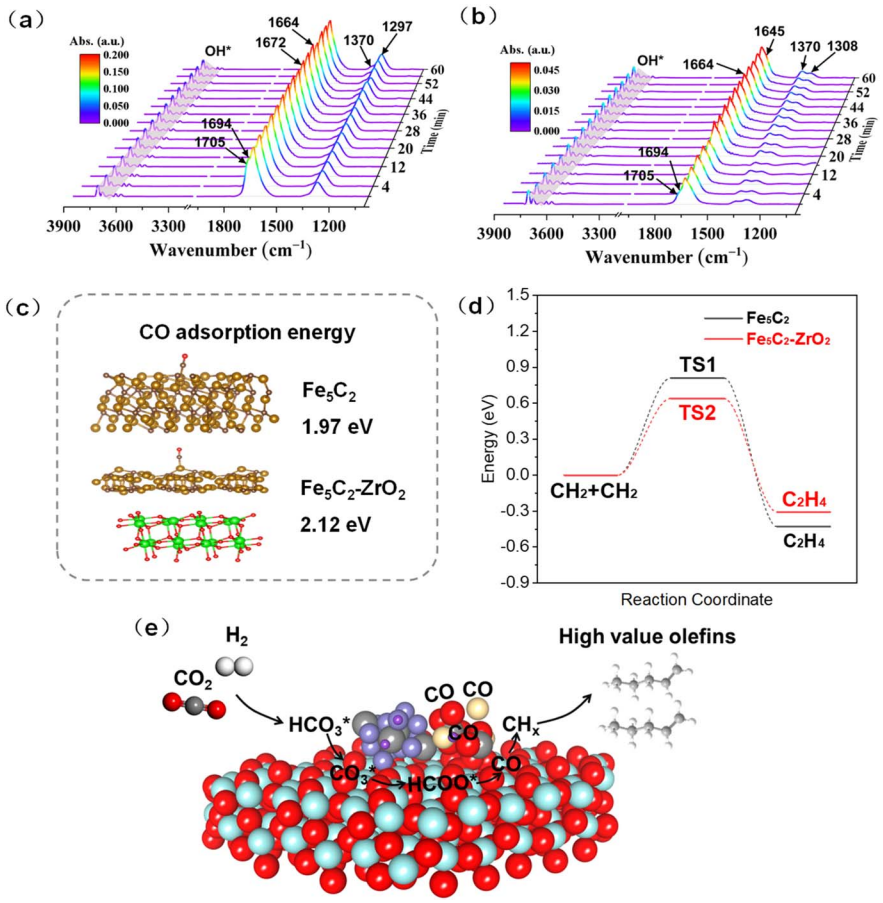

Fig. 7 *In situ* DRIFTS of CO_2 hydrogenation to LAOs over the Na/FeMn/ZrO_2 catalyst. (a) $H_2/CO_2 = 3$, 200 °C, 30 mL min^{-1} (b) $H_2/CO_2 = 3$, 320 °C, 30 mL min^{-1} (reduced conditions: 400 °C, H_2, 30 mL min^{-1}). (c) CO adsorption energy at the Fe_5C_2 and Fe_5C_2–ZrO_2 interfaces. (d) Comparison of energy barriers of CH_2 + CH_2 over Fe_5C_2 and the Fe_5C_2–ZrO_2 interface. (e) Reaction scheme for high-value olefin synthesis from CO_2 hydrogenation over the Na/FeMn/ZrO_2 catalyst.

sites promoted the RWGS and FTS reactions of CO_2 hydrogenation. CO_2 was adsorbed on the active sites as carbonate species, which underwent hydrogenation to bicarbonate and subsequently to formate species, followed by further hydrogenation yielding dissociated CO intermediates. The CO generated *via* RWGS was further hydrogenated into CH_x^* species on iron carbide active sites, and then proceeded to C–C coupling for the formation of high-value olefins. Importantly, Fe_5C_2–ZrO_2 significantly enhanced CO adsorption capacity, enriching CO intermediates on Fe_5C_2 active sites and selectively promoting C–C coupling reactions, thereby producing high-value olefins.

Conclusions

In this work, a Na/FeMn/ZrO_2 catalyst featuring an Fe_5C_2–ZrO_2 interfacial structure was prepared *via* a covalent anchoring strategy. This catalyst exhibited excellent LAOs selectivity and O/P ratio in the directed hydrogenation of CO_2 to LAOs, achieving a LAOs/C_{4+} selectivity of 68% and an O/P ratio of 5.1. During reduction, Mn and ZrO_2 promoted oxygen vacancy formation through lattice oxygen dissociation, thereby enhancing CO_2 adsorption and C–O bond activation. The strong interaction between Fe species and $MnCO_3$, driven by the electronic effect of alkaline earth metal carbonates, effectively improved the catalytic activity. Concurrently, the Fe_5C_2–ZrO_2 interfaces demonstrated stronger CO adsorption capacity. Elevated CO partial pressure on the Fe_5C_2 surface facilitated the C–C coupling reaction. The synergistic interplay of multiple active sites suppressed the secondary hydrogenation of primary olefins while effectively promoting the generation of LAOs.

Author contributions

Kangzhou Wang: investigation, formal analysis, writing – original draft. Tong Liu: investigation. Pengqi Hai: software. Shunnosuke Fujii: investigation. Chufeng Liu: formal analysis. Hanyao Song: methodology. Caixia Zhu: investigation. Guangbo Liu: supervision. Jianli Zhang: funding acquisition. Zhou-jun Wang: writing – review & editing. Noritatsu Tsubaki: writing – review & editing.

Conflicts of interest

There are no conflicts to declare.

Data availability

The authors confirm that the data supporting the findings of this study are available within the article and its supplementary information (SI). Supplementary information is available. See DOI: https://doi.org/10.1039/d5sc08926c.

Acknowledgements

This work was financially supported in part by the National Natural Science Foundation of China (22368041 and 22378017), the Key Research and Development Program of Ningxia (Talent-Introduction Program, 2023BSB03061), and the Ningxia Natural Science Foundation (2024AAC03049). P. Hai acknowledges the Hefei Advanced Computing Center.

Notes and references

1 G. A. Meehl, W. M. Washington, W. D. Collins, J. M. Arblaster, A. Hu, L. E. Buja, W. G. Strand and H. Teng, *Science*, 2005, **307**, 1769–1772.
2 H. He, R. J. Kramer, B. J. Soden and N. Jeevanjee, *Science*, 2023, **382**, 1051–1056.
3 K. Wang, H. Oe, Y. Nakaji, Y. Wang, T. Nakaji-Hirabayashi and N. Tsubaki, *Chem*, 2024, **10**, 419–426.
4 W. Zhou, K. Cheng, J. Kang, C. Zhou, V. Subramanian, Q. Zhang and Y. Wang, *Chem. Soc. Rev.*, 2019, **48**, 3193–3228.
5 C. Y. Sun, W. Li and H. Q. Wang, *Rare Met.*, 2024, **43**, 410–412.
6 K. Wang, Z. Li, X. Gao, Q. Ma, J. Zhang, T. Zhao and N. Tsubaki, *Environ. Res.*, 2024, **242**, 117715.
7 N. Liu, J. Wei, J. Xu, Y. J. Yu, Y. Han, K. Wang, J. I. Orege, Q. Ge and J. Sun, *Appl. Catal., B*, 2023, **328**, 122476.
8 M. Cui, Q. Qian, J. Zhang, Y. Wang, B. B. A. Bediako, H. Liu and B. Han, *Chem*, 2021, **7**, 726–737.
9 T. Liu, K. Wang, Z. Liu, H. Feng, C. Liu, H. Song, D. Liang, T. Yang, K. Liu, X. Gao, J. Zhang and N. Tsubaki, *AIChE J.*, 2025, e70051.
10 X. Wang, Y. Man, R. Zhang, C. Cui, K. Wang and Z. Wang, *Chem. Eng. J.*, 2025, **505**, 159458.
11 D. Wang, Z. Xie, M. D. Porosoff and J. G. Chen, *Chem*, 2021, **7**, 2277–2311.
12 Y. Jiang, K. Wang, Y. Wang, Z. Liu, X. Gao, J. Zhang, Q. Ma, S. Fan, T. Zhao and M. Yao, *J. CO2 Util.*, 2023, **67**, 102321.
13 J. Wei, Q. Ge, R. Yao, Z. Wen, C. Fang, L. Guo, H. Xu and J. Sun, *Nat. Commun.*, 2017, **8**, 15174.
14 S. Kattel, P. J. Ramírez, J. G. Chen, J. A. Rodriguez and P. Liu, *Science*, 2017, **355**, 1296–1299.
15 B. Yao, T. Xiao, O. A. Makgae, X. Jie, S. Gonzalez-Cortes, S. Guan, A. I. Kirkland, J. R. Dilworth, H. A. Al-Megren, S. M. Alshihri, P. J. Dobson, G. P. Owen, J. M. Thomas and P. P. Edwards, *Nat. Commun.*, 2020, **11**, 6395.
16 T. Liu, K. Wang, W. Zhang, W. Song, F. Bo, C. Li, Q. Ma, X. Gao, T. Zhao and J. Zhang, *J. Environ. Chem. Eng.*, 2024, **12**, 113885.
17 J. Wang, Y. Xu, G. Ma, J. Lin, H. Wang, C. Zhang and M. Ding, *ACS Appl. Mater. Interfaces*, 2018, **10**, 43578.
18 S. Wang, T. Wu, J. Lin, Y. Ji, S. Yan, Y. Pei, S. Xie, B. Zong and M. Qiao, *ACS Catal.*, 2020, **10**, 6389–6401.
19 B. Liu, J. Liang, X. Gao, Q. Ma, J. Zhang and T. Zhao, *Fuel*, 2022, **326**, 125054.
20 J. Liang, J. Liu, L. Guo, W. Wang, C. Wang, W. Gao, X. Guo, Y. He, G. Yang, B. Liang and N. Tsubaki, *Nat. Commun.*, 2024, **15**, 512.
21 T. Witoon, V. Lapkeatseree, T. Numpilai, C. K. Cheng and J. Limtrakul, *Chem. Eng. J.*, 2022, **428**, 131389.
22 L. Wang, Y. Han, J. Wei, Q. Ge, S. Lu, Y. Mao and J. Sun, *Appl. Catal., B*, 2023, **328**, 122506.

23 J. Zhu, M. Mu, Y. Liu, M. Zhang, G. Zhang, Z. Cheng, B. Yin, A. C. K. Yip, C. Song and X. Guo, *Chem. Eng. Sci.*, 2023, **282**, 119228.
24 K. Wang, Z. Li, T. Liu, X. Gao, T. Yang, K. Liu, X. Gao, Q. Ma, J. Zhang, T. Zhao and N. Tsubaki, *ACS Catal.*, 2024, **14**, 17469–17479.
25 W. Tu, C. Sun, Z. Zhang, W. Liu, H. S. Malhi, W. Ma, M. Zhu and Y. F. Han, *Appl. Catal., B*, 2021, **298**, 120567.
26 M. Xu, X. Liu, G. Song, Y. Cai, B. Shi, Y. Liu, X. Ding, Z. Yang, P. Tian, C. Cao and J. J. Xu, *Catal*, 2022, **413**, 331–341.
27 H. Liu, L. Jiang, J. Khan, X. Wang, J. Xiao, H. Zhang, H. Xie, L. Li, S. Wang and L. Han, *Angew. Chem., Int. Ed.*, 2023, **135**, e202214988.
28 B. Liu, Z. Wang, T. Wei, Z. Liu and J. Li, *J. Environ. Chem. Eng.*, 2023, **11**, 110186.
29 D. Ma, Y. Xu, P. Zhai, Y. Deng, J. Xie, X. Liu and S. Wang, *Angew. Chem., Int. Ed.*, 2020, **59**, 21736–21744.
30 J. Zhu, P. Wang, X. Zhang, G. Zhang, R. Li, W. Li, T. P. Senftle, W. Liu, J. Wang, Y. Wang, A. Zhang, Q. Fu, C. Song and X. Guo, *Sci. Adv.*, 2022, **8**, eabm3629.
31 Y. Fu, C. C. Amoo, H. Qi, H. Liu, L. Zhu, P. Lu, R. Yang, C. Xing, S. Wang and J. Sun, *Chem. Eng. J.*, 2022, **438**, 135597.
32 Z. Zhang, G. Huang, X. Tang, H. Yin, J. Kang, Q. Zhang and Y. Wang, *Fuel*, 2022, **309**, 122105.
33 B. Liang, H. Duan, T. Sun, J. Ma, X. Liu, J. Xu, X. Su, Y. Huang and T. Zhang, *ACS Sustainable Chem. Eng.*, 2019, **7**, 925–932.
34 J. I. Orege, N. Liu, C. C. Amoo, J. Wei, Q. J. Ge and J. Sun, *J. Energy Chem.*, 2023, **80**, 80614–80624.
35 J. I. Orege, J. Wei, Y. Han, M. Yang, X. Sun, J. Zhang, C. C. Amoo, Q. Ge and J. Sun, *Appl. Catal., B*, 2022, **316**, 121640.
36 Z. Li, W. Wu, M. Wang, Y. Wang, X. Ma, L. Luo, Y. Chen, K. Fan, Y. Pan, H. Li and J. Zeng, *Nat. Commun.*, 2022, **13**, 2396.
37 H. Ren, H. Yang, J. Xin, C. Wu, H. Wang, J. Zhang, X. Bu, G. Yang, J. Li, Y. Sun and P. Gao, *Appl. Catal., A*, 2024, **358**, 124440.
38 Q. Yang, E. A. Fedorova, D. B. Cao, E. Saraçi, V. A. Kondratenko, C. R. Kreyenschulte, H. Lund, S. Bartling, J. Wei, D. E. Doronkin and J. D. Grunwaldt, *Nat. Catal.*, 2025, **8**, 595–606.
39 Z. Ni, X. Chen, L. Su, H. Shen, Y. Jiang, C. Feng and C. Yin, *ACS Sustainable Chem. Eng.*, 2025, **13**, 6335–6347.
40 X. Li, Z. Yang, L. Zhang, Z. He, Y. Yan, J. Ran and Z. C. Kadirova, *Fuel*, 2022, **322**, 124122.
41 H. Yang, Y. Dang, X. Cui, X. Bu, J. Li, S. Li, Y. Sun and P. Gao, *Appl. Catal., B*, 2023, **321**, 122050.
42 H. Pitayachinchot, P. Reubroycharoen, P. Prasassarakich, T. Yokoi, Y. Shen, M. Gao and C. Ngamcharussrivichai, *Environ. Technol. Innov.*, 2025, **38**, 104162.
43 H. Ma, Y. Cai, Y. Jiao, X. Liu, J. Liu, W. Guo, X. Liu, Y. Li and X. Wen, *J. Am. Chem. Soc.*, 2025, **147**, 41452–41461.
44 J. I. Orege, N. Liu, C. C. Amoo, J. Wei, Q. J. Ge and J. Sun, *J. Energy Chem.*, 2023, **80**, 80614–80624.
45 S. Z. Ghorbaei and H. A. Ebrahim, *Appl. Energy*, 2020, **277**, 115604.
46 J. Huang, S. Jiang, M. Wang, X. Wang, J. Gao and C. Song, *ACS Sustainable Chem. Eng.*, 2021, **9**, 7891–7903.
47 X. Ai, Y. Zhang, Y. Zhao, J. Hong, C. Liu and J. Li, *Fuel*, 2025, **384**, 133958.
48 D. Ma, Y. Xu, P. Zhai, Y. Deng, J. Xie, X. Liu and S. Wang, *Angew. Chem., Int. Ed.*, 2020, **59**, 21736–21744.
49 J. Han, Y. Han, J. Yu, Y. Sun, X. Cui, Q. Ge and J. Sun, *Angew. Chem., Int. Ed.*, 2025, **64**, e202420621.
50 J. Li, X. Yuan, F. Tian, M. Wang, T. Hu, G. Xiong and X. Wang, *Appl. Catal., A*, 2024, **681**, 119781.
51 M. Qing, Y. Yang, B. Wu, J. Xu, C. Zhang, P. Gao and Y. Li, *J. Catal.*, 2011, **279**, 11–22.
52 Q. Chang, J. Li, H. Suo, M. Qing, H. Wang, C. Zhang, X. Wen, H. Xiang, Y. Yang and Y. Li, *Catal. Today*, 2024, **431**, 114605.
53 Z. Yang, Z. Zhang, Y. Liu, X. Ding, J. Zhang, J. Xu and Y. Han, *Appl. Catal., B*, 2021, **285**, 119815.
54 X. Gong, Y. Liu, R. He, X. Xu, Z. Han, J. Chen, B. Feng, Z. J. Wang and A. Xing, *ChemCatChem*, 2024, **16**, e202301341.
55 K. S. Belthle, W. F. Martin and H. Tüysüz, *ChemCatChem*, 2024, **16**, e202301218.
56 H. Yu, C. Wang, X. Xin, Y. Wei, S. Li, Y. An, F. Sun, T. Lin and L. Zhong, *Nat. Commun.*, 2024, **15**, 5143.
57 Z. Cai, N. Cao, F. Zhang, X. Lv, K. Wang, Y. He, Y. Shi, H. B. Wu and P. Xie, *Appl. Catal., B*, 2023, **325**, 122310.
58 G. Song, Q. Jiang, Y. Zhai and D. Liu, *Chem. Eng. Sci.*, 2023, **280**, 119037.
59 W. Song, K. Wang, Y. Xing, W. Zhang, T. Liu, F. Bo, J. Liang, X. Gao, Q. Ma, T. Zhao and J. Zhang, *Appl. Catal., A*, 2024, **688**, 120001.
60 Q. Chang, C. Zhang, C. Liu, Y. Wei, A. V. Cheruvathur, A. I. Dugulan, J. W. Niemantsverdriet, X. Liu, Y. He, M. Qing, L. Zheng, Y. Yun and Y. Yang, *ACS Catal.*, 2018, **8**, 3304–3316.
61 G. B. Raupp and W. N. Delgass, *J. Catal.*, 1979, **58**, 348–360.
62 G. Yu, B. Sun, Y. Pei, S. Xie, S. Yan, M. Qiao, K. Fan, X. Zhang and B. Zong, *J. Am. Chem. Soc.*, 2010, **132**, 935–937.
63 Q. Yang, V. A. Kondratenko, S. A. Petrov, D. E. Doronkin, E. Saraçi, H. Lund, A. Arinchtein, R. Kraehnert, A. S. Skrypnik, A. A. Matvienko and E. V. Kondratenko, *Angew. Chem., Int. Ed.*, 2022, **61**, e202116517.
64 Q. Yang, H. Lund, S. Bartling, F. Krumeich, A. S. Skrypnik and E. V. Kondratenko, *J. Catal.*, 2023, **426**, 126–139.
65 G. P. Laan and A. A. Beenackers, *Catal. Rev.*, 1999, **41**, 255–318.
66 E. de Smit and B. M. Weckhuysen, *Chem. Soc. Rev.*, 2008, **37**, 2758–2781.
67 Y. Xu, P. Zhai, Y. Deng, J. Xie, X. Liu, S. Wang and D. Ma, *Angew. Chem., Int. Ed.*, 2020, **59**, 21736–21744.
68 B. Liu, S. Geng, J. Zheng, X. Jia, F. Jiang and X. Liu, *ChemCatChem*, 2018, **10**, 4718–4732.
69 R. Ye, J. Ding, T. R. Reina, M. S. Duyar, H. Li, W. Luo, R. Zhang, M. Fan, G. Feng, J. Sun and J. Liu, *Nat. Synth.*, 2025, **4**, 288–302.
70 M. K. Khan, P. Butolia, H. Jo, M. Irshad, D. Han, K. W. Nam and J. Kim, *ACS Catal.*, 2020, **10**, 10325–10338.
71 Q. Xu, X. Xu, G. Fan, L. Yang and F. Li, *J. Catal.*, 2021, **400**, 355–366.